MICROMEGAS
Beam Test 2008 - Analysis & Results

C. Adloff, A. Espargilière*, Y. Karyotakis

Abstract

Prototypes of MICROMEGAS chambers using bulk technology and equipped with analog readout have been tested in particle beams. Measurements of detector gain, efficiency and multiplicity are presented. Disparities of gain and efficiency are presented as well. Threshold dependencies of efficiency and multiplicity are also shown. The chambers behaviour in high energy hadronic showers is briefly addressed in the last section.

1 Introduction

1.1 Framework

Future linear e^+e^- colliders at Terascale energies (like ILC or CLIC) will be the probes for new physics. Using LHC results as a starting point they would be able to get unprecedented measurements on Higgs physics but also on Super Symmetry and other Standard Model extensions.

Such high energies require very demanding detectors which are currently developed by many international collaborations in intensive R&D activities. Our team at LAPP takes part in this effort by developing active layers for digital hadronic calorimetry complying with the needs of a detector using the Particle Flow Algorithm (PFA) [1]. The main basic needs are very thin active layers, to minimize the hadronic calorimeter (HCAL) thickness, and a high segmentation, to allow precise shower identification and single particle reconstruction. The high segmentation together with the large area to instrument leads to a huge number of readout channels [1] and therefore an enormous amount of data to handle and store. To balance this, an idea is to have a (semi-) digital readout so that each channel signal would be encoded with 1 or 2 bits instead of 12 or more, leading to the differentiation between Analog HCAL (AHCAL) and Digital HCAL (DHCAL).

The solution studied here at LAPP is toward a DHCAL for the SiD detector concept [2] and consists in an active layer made of MICRO-MEsh GAseous Structure (MICROMEGAS) chambers with a specific thickness of only 3.2 mm and 1 cm^2 segmentation.

1.2 MICROMEGAS

The MICROMEGAS was introduced in 1996 [3] as a fast signal, position-sensitive, radiation hard gaseous detector. It consist of a gas chamber, filled with a noble gas based mixture, and divided by a conductive mesh into two gaps called "drift gap" and "amplification gap". The drift gap lies between the drift electrode and the mesh, and is usually a few millimeters thick. The amplification gap is located between the mesh and the anode and is only about a few tens of micron thick.

A proper electric field is defined in each gap by the voltage applied to the electrodes. The field in the drift space is quite low (around 100 V/cm) and is meant to drift free electrons to the mesh. The field in the amplification gap is very high (around 40 000 V/cm) and catch the free electrons from the drift gap to strongly accelerate them along the small amplification gap. They then acquire enough energy to ionize surrounding gas, freeing more and more electrons which are accelerated the same way, thus forming an avalanche and leading to a measurable electric signal on the anode and on the mesh. A scheme summarizing MICROMEGAS principle is displayed on figure 1

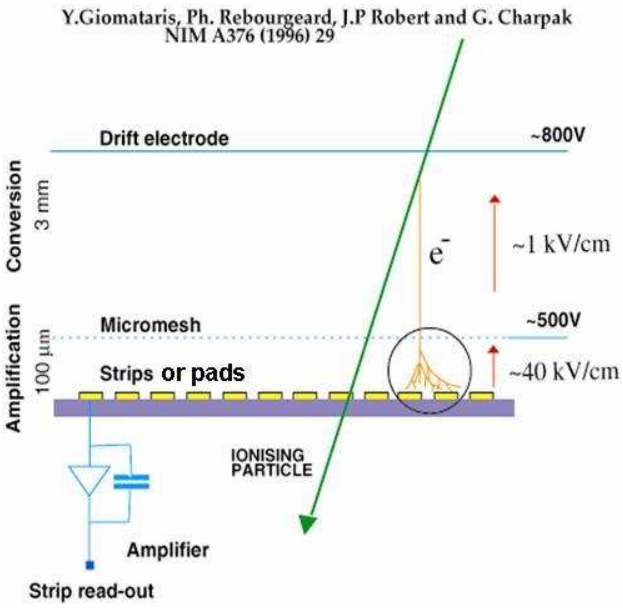

Figure 1: Scheme of MICROMEGAS principle.

2 Experimental Setup

2.1 Prototypes

Each prototype consists of a bulk MICROMEGAS chamber [4] with a 3 mm drift gap and a 128 μm amplification gap. The drift cathode is a 5 μm thick

*corresponding author
[1] $\approx 3 \cdot 10^7$ channels for SiD HCAL

copper foil fixed on a 75 μm thick Kapton film. The whole is glued on a 2 mm thick steel plate, forming the device's lid. The copper cathode attached to the steel cover plate are part of the absorber and therefore do not contribute to the HCAL active layer's thickness. The 3 mm drift gap is ensured by a 3 mm resin frame enclosing the chamber and providing the gas inlet and outlet. The gas used for the presented tests is an Ar/iC_4H_{10} (95/5) mixture.

The mesh is an industrial micro woven stainless steel mesh made of 30 μm diameter wires interwoven at a pitch of 80 μm. The mesh is held by 128 μm high, 300 μm diameter pillars laid out on a square lattice with a 2 mm pitch. The anode plane consists of $0.98\times0.98\,cm^2$ pads spaced by 200 μm lying on the detector's PCB. The PCB is 4 layers, class 4, 1.6 mm thick.

Four prototypes with analog readout have been built and then tested at CERN. Three of them have a $6\times16\,cm^2$ active area (figure 2) and the last one is four times larger with a $12\times32\,cm^2$ active area. In the following, the three small chambers will be referred to as CH0, CH1 and CH2 and the large one as CH3. Since the analysis is based on track reconstruction through the four chambers the results for CH3 only concerns the central region in the shadow of the three small ones.

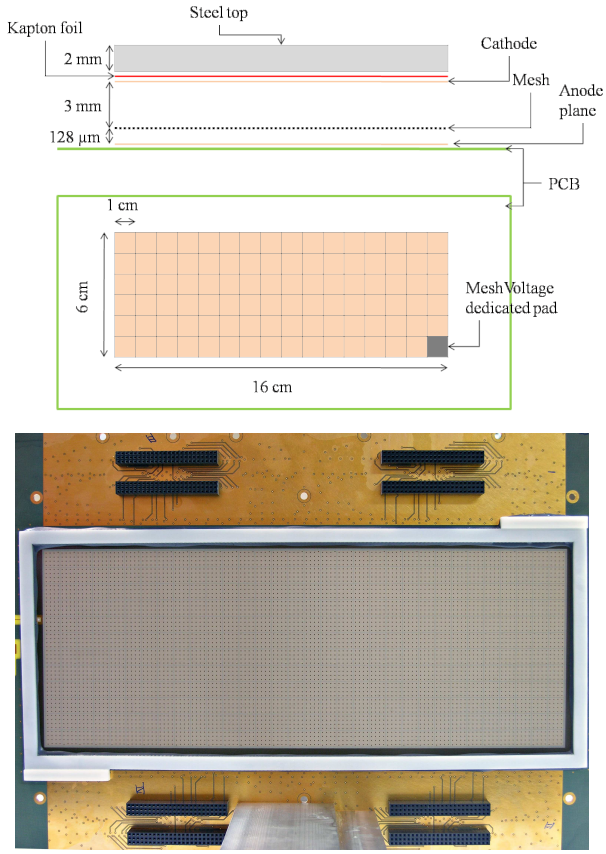

Figure 2: Analog readout prototypes. The drawing give CH0 to CH2 dimensions but can be straightforwardly extended to CH3 since the only difference for CH3 is the larger size (12×32 pad instead of 6×16) and a sidelong mesh voltage 4 mm^2 pad. The photography shows CH3 before its lid was glued, the mesh voltage spot is visible on the middle right of the frame.

2.2 Readout System

2.2.1 Description

The analog anode readout was provided by seven 613V boards[2] from CEA, equipped with 6 GASSIPLEX [5] chips each, offering a total of 672 readout channels for the whole analog detector stack. GASSIPLEX chips, when triggered, gather the signal from every channel and build one single multiplexed differential output with nominal conversion factor of 3.6 mV/fC and a peaking time of 1.2 μs. The 613V boards were modified to provide the anode grounding by soldering 1 MΩ resistors between each input and the nearby ground leg.

The multiplexed signal from GASSIPLEX 613V boards was acquired by CAEN V550 10 bits ADC VME modules sequenced by a CAEN V551B C-RAMS sequencer VME module. The data were recorded thanks to the CENTAURE acquisition and monitoring software from SUBATECH[3].

2.2.2 Calibration

A calibrated pulse has been injected through the GASSIPLEX internal test capacitance. The output is stored for further analysis. This process is repeated for three value of the input charge (voltage of 250, 80 and 25 mV). For any particular charge injection, the spectrum shows a peak clearly above pedestal (see fig. 3).

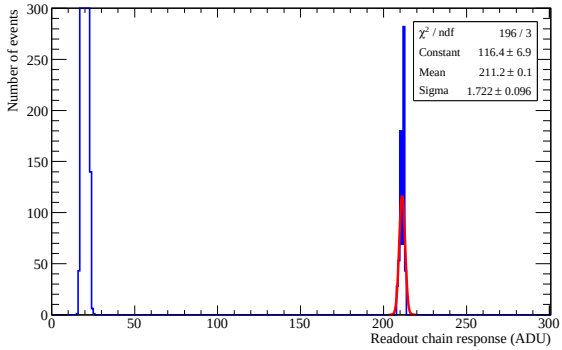

Figure 3: Response of the readout chain to an injected charge of 40 fC.

Plotting this peak's mean value versus the injected charge gives a straight line (see fig. 4) which slope corresponds to the electronic gain in ADU[(4)] per fC.

The gains for all channels of each board are gathered on the histogram fig. 5.

The overall gain disparity shows a 2.5% disparity (see Fig. 5), thus no intercalibration have been applied and a global conversion factor for all readout channels have been set. The gain for boards 55, 30

[2]CEA DAPNIA Board N°613V, 96 channels, 6 GASSIPLEX chips 0.7 v3 designed by Philippe ABBON.

[3]Online documentation:
http://www-subatech.in2p3.fr/ẽlectro/infoaq/CENTAURE21lv85/main_centaure.html

[4]ADU: Analog to Digital Unit

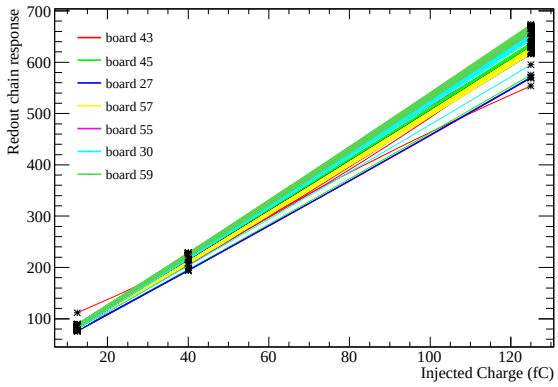

Figure 4: Calibration peak versus injected charge.

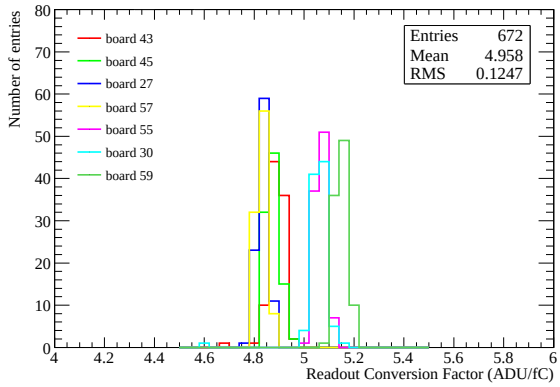

Figure 5: Electronic gain for all 613V boards.

and 59 is 4% higher than the average of the other boards and thus induces a 2% increase of the average gain. To avoid an overestimation of the gain of te chambers CH0, 1 and 2 these values where excluded from the global convertion factor computation. The resulting value of the global conversion factor of the GASSIPLEX readout chain measured using the internal test capacitor is then (4.85±0.07) ADU/fC. The final value was set to 4.69±0.25 ADU/fC because of 3.29% difference between internal and external test capacitor (see [6] for details about this).

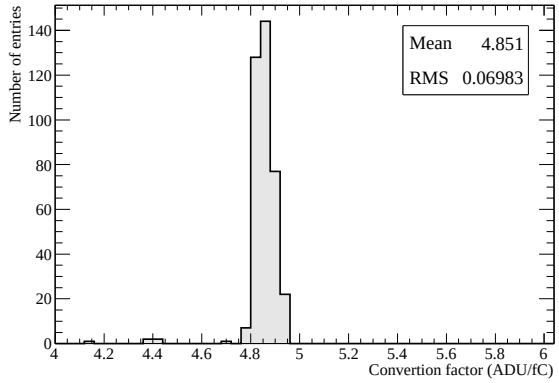

Figure 6: Electronics gain of GASSIPLEX 613V boards for CH0, CH1, CH2 and first sector of CH3.

2.3 Beam Test Setup

In a metallic structure, each chamber has been fixed on a plastic frame and aligned with each other. In front of the chambers, three scintillator paddles have been fixed in the structure and used for the trigger (see fig. 7). The ADC modules and the high voltage power supply have been housed in a VME crate, just nearby the structure to minimize the wire's length. The mesh voltages have been respectively for CH0, CH1, CH2 and CH3, 420 V,420 V, 430 V, and 410 V, the drift voltage has been 50 V higher.

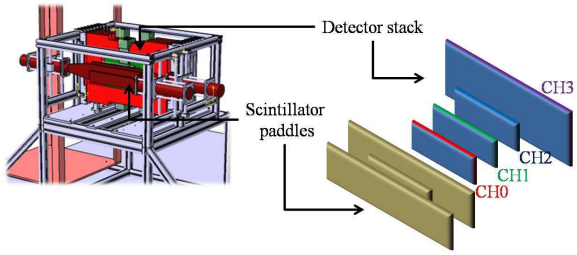

Figure 7: Scheme of the beam test structure, right side focuses on the detectors and scintillators paddle layout.

2.4 Particle Sources

2.4.1 CERN/SPS, H2 beam line

The Super Proton Synchrotron (SPS) provides a 400 GeV/c proton beam for fixed target experiments. Data have been taken from a secondary 200 GeV/c negative muon beam. The beam has been available during a 9 s spill period every machine cycle. Each machine cycle has lasted for 33 s during night time and 48 s during day time. The beam has been intense enough to saturate the acquisition rate at about 130 events/ s.

2.4.2 CERN/PS, T9 beam line

The Proton Synchrotron (PS) delivers a 28 GeV/c proton beam for injection in SPS and CERN's East Area's Fixed target experiments. Data have been recorded from a secondary 7 GeV/c positive pion beam. The beam has been available during one or a few 0.4 s spill periods every machine cycle. A machine cycle has lasted for a variable time around 40 s. The number of spill period has been variable between 1 and 3. The beam has also been intense enough to saturate the acquisition rate.

3 Data, Event Tagging

In the following, a hit is defined as a channel response exceeding a 27 ADU threshold (7 ADU or 1.5 fC above pedestal). It corresponds roughly to the saddle point between pedestal and signal or also to the signal induced by one single primary electron (with a gain of 10^4). Event have been categorized regarding some basic criteria on the hit distribution. The categories are enumerated and described below. Dedicated data

file have been produced for each category in order to ease the analysis.

1. **Platinum Events:** events in which each of the four chambers shows a single hit. There's no assumption here about the position of those hits within the chambers. Those events have been used for gain and pedestal studies.

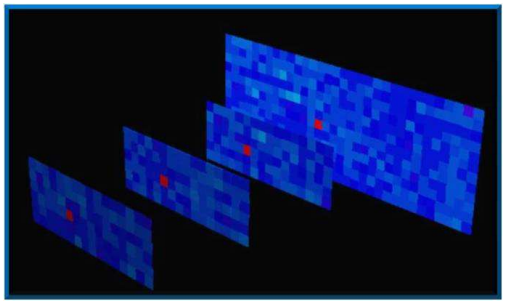

Figure 8: Example of Platinum event.

2. **Golden Events:** events in which at least three out of the four chambers show a single hit, without assumption about their position, and no condition at all on the last chamber. Those events have been used for efficiency and multiplicity studies.

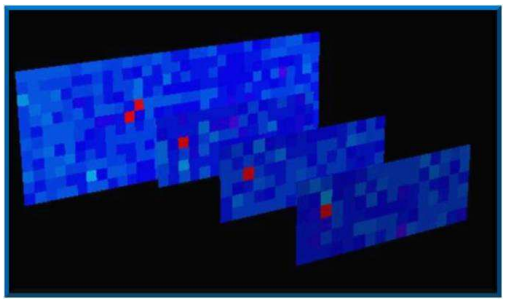

Figure 9: Example of Gold event.

3. **Silver Events:** in those events, several hits are allowed per chamber but only in a 3×3 pad area around the strongest one, it is possible to apply this condition on all chambers (platinum like) or on three of them (gold like). Multiple hits allow computing a weighted position for the hit, thus increasing tracking accuracy. Such events have been used to check chamber alignment.

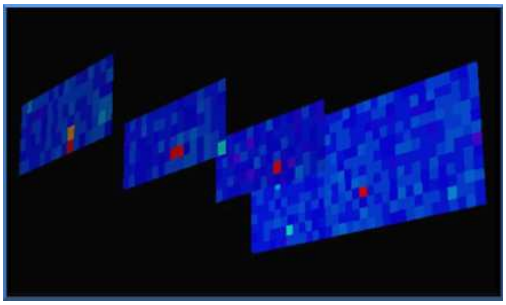

Figure 10: Example of Silver event.

4 Noise Conditions and Gain Disparity

Platinum events have been used to build the landau distribution of the particle signal in single channels. The statistics has been sufficient to fit a landau function on the data from every pad of the small chambers(figure 11) and of the central region of CH3 in the shadow of the small ones.

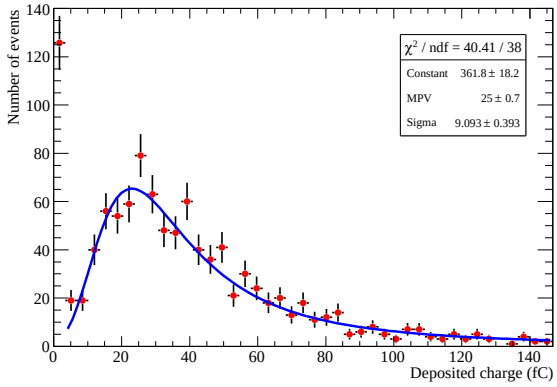

Figure 11: Response from a single readout channel, the pedestal has been scaled to fit in the vertical range.

Noise Conditions The pedestal has been at 20 ADU. Its width has been obtained as the sigma of a gaussian fit and showed an average value, over 672 channels, of 1.5 ADU corresponding to 0.3 fC or 2000 e^- (see fig. 19). This can be considered as very good noise conditions.

Gain Disparity A map of the gain of each detector has been built up (fig 21), and the gain relative distribution has been measured (fig. 12). The normalized gain distribution has shown a 11% r.m.s. disparity. The absolute gain distribution of each individual chamber is diplayed in figure 22.

The relative disparities of each chamber's gain are gathered in table 1. One can notice that the higher the gain, the lower the relative gain disparity. This trend shall be examined more precisely with further measurements because it is not respected in November data in which the values are respectively: 9.12%, 11.69%, 13.18% for CH1, CH2 and CH3 with the same voltage settings.

Chamber	V_{mesh}	Gain disp.
CH0	420 V	8.13%
CH1	420 V	8.23%
CH2	430 V	7.69%
CH3	410 V	12.98%

Table 1: Gain disparity for each chamber.

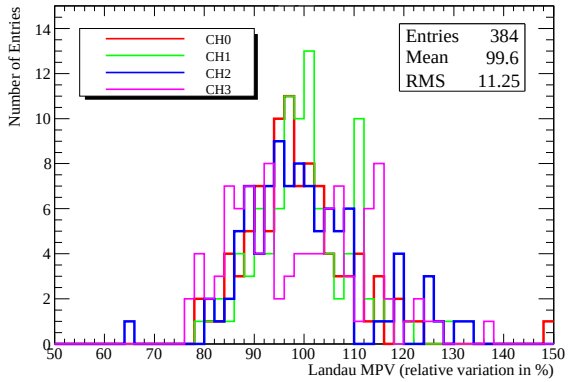

Figure 12: Normalized gain distribution for the four chambers.

5 Chambers Alignment

The precise position of each chamber relatively to each other has been computed using particle tracks. Silver Events were used to compute the hit position by considering the mean between the actual hits weighted by their corresponding deposited energy. This method is thought to be more accurate than considering pad centres as the hit position. After hit positions are computed within a particular event, a straight line is fitted through them. Afterwards, the distance, separately along x and y axis, between effective hits and the fitted straight line is computed and plotted in figure 20. This study has unlighted a 2 mm misalignment along x axis of CH3, 1.6 mm along y axis for CH1 and 5.7 mm for CH2. An offline correction of the chambers position in the analysis programs can't prevent from inefficiencies biases due to misalignment because the tracking capability of such a stack of detector is too limited. The particle position can only be considered at the centre of the pad. Hence, a small misalignment lead some particles, passing on pad borders, to induce signal on a pad aside the expected one but there is no way to rebuild the particle tracks with enough precision to identify such events (see scheme in figure 13). This information has obliged us to perform efficiency measurements with a 3×3 pad target area and to omit the border pads of the chambers.

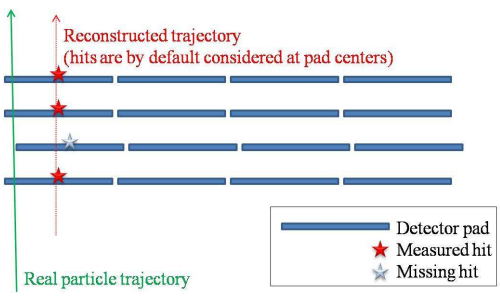

Figure 13: Geometrical inefficiency

6 Noise Contribution

To perform efficiency or multiplicity measurements, hits have been searched in a 3 × 3 pad area around a predicted position. There is a probability that a counted hit came from some noise instead of physical signal. This contribution needs to be evaluated to correct the raw measurements. For each processed event, the target area has been taken as the unit area. The number of hits outside the target area has been normalized to the unit area and stored. The mean of this number over all the events is then the average number of fortuitous hits per area unit and per event. If the detectors had been completely noisy (*eg* by setting the threshold below pedestal) this number shall then be about 9, but for a reasonable threshold the average number of fortuitous hits per unit surface and per event is expected to be relatively low and shall then coincide with the probability of counting at least one fortuitous hit in a 3×3 pad target area, denoted p hereafter. This assumption has been made for the estimation of the noise contribution to efficiency and multiplicity measurements.

Another possibility is to compute the single pad fortuitous hit probability p_1 and then deduce the corresponding 3×3 pad probability of spotting at least one hit. This probability is deduced from combinatorial at the second order in p_1 through:

$$p = 9p_1(1-p_1)^8 + 36p_1^2(1-p_1)^7 + o(p_1^3)\,, \quad (1)$$

with error:

$$\begin{aligned}\Delta p &= \Delta(9\cdot p_1(1-p_1)^8) + \Delta(36\cdot p_1^2(1-p_1)^7) \\ &= 9\cdot p_1(1-p_1)^8\left(\frac{\Delta p_1}{p_1} + 8\frac{\Delta p_1}{(1-p_1)}\right) \\ &+ 36\cdot p_1^2(1-p_1)^7\left(2\frac{\Delta p_1}{p_1} + 7\frac{\Delta p_1}{(1-p_1)}\right) \quad .(2)\end{aligned}$$

Chamber	direct	computed
CH0	(1.30±0.08)%	(1.71±0.28)%
CH1	(1.33±0.08)%	(1.87±0.29)%
CH2	(2.00±0.10)%	(2.60±0.33)%
CH3	(1.65±0.09)%	(1.39±0.26)%

Table 2: Comparison between 3×3 pad fortuitous hit probability direct measurement and 3×3 pad fortuitous hit probability computation from single pad noise.

The results are compatible but the error margin on the computed values are higher than for the directly measured ones and the values are mainly higher as well. This difference can be explained by the fact that by looking at only one pad to search for noise contribution, any secondary hit due to signal multiplicity is automatically considered as noise. Computed values are therefore biased by the hit multiplicity. The direct method has been kept to perform noise estimation and make correction to efficiency and multiplicity. A quantity Q, standing either for efficiency or multiplicity, is corrected for noise contribution using the simple formula:

$$Q_{corr} = Q\cdot(1-p)\,. \quad (3)$$

7 Efficiency

In order to measure the efficiency of a given chamber, the three others have been considered as reference and a sub-sample of golden events has been selected with stronger conditions:

1. the hit threshold for the three reference chambers has been risen to 12.5 fC to completely avoid fortuitous hits,
2. the three reference chambers must show one single hit,
3. the three hits must be aligned.

If an event fulfilled those criteria, the so-obtained track has been extrapolated to the tested chamber to predict a hit position. This position has been stored in a 2D histogram (upper left map in figure 23). Afterwards, a hit[5] has been searched in a 3×3 pad area around this expected hit. When found, the predicted hit position has been stored in a second 2D histogram (upper right map in fig 23). When all events have been processed, the second histogram has been divided by the first (counted hits/expected hits), resulting in a 2D histogram representing the efficiency map of the chamber (lower left map in figure 23). The error on efficiency is computed through the usual formula:

$$\Delta\epsilon \quad = \quad \sqrt{\frac{\epsilon \cdot (1-\epsilon)}{N_{tot}}}\,, \tag{4}$$

where ϵ is the efficiency and $\Delta\epsilon$ its error, N_{tot} is the total number of events in the selected sub-sample.

For each chamber the raw efficiency[6], the noise corrected efficiency and the channel to channel disparity of the raw efficiency at a 1.5 fC threshold are gathered in table 7. A test of efficiency measurement using a 1 pad target area was also performed and gave much worse results, as expected from the misalignment. Measurements taking the borders pad were also performed but, as expected, the misalignment issues on border pads could not be balanced by the 3×3 pad target area.

Ch.	Raw eff.	Noise corr. eff.	Disp.
CH0	(99.0±0.1)%	(97.7±0.1)%	0.79%
CH1	(99.0±0.1)%	(97.7±0.1)%	0.51%
CH2	(93.0±0.1)%	(91.2±0.1)%	3.74%
CH3	(98.8±0.1)%	(97.2±0.1)%	0.75%

Table 3: Efficiency measurements for a 1.5 fC threshold.

8 Multiplicity

The same sub-sample of golden events as for efficiency measurement has been used. The straight line formed by the three hits of the reference chambers predict a hit position in the tested chamber. The number of hits found in the 3 × 3 pad area centred at the predicted hit position has been counted. The average of this number (excluding the zeros) over all the processed events is the multiplicity of the chamber. It can be formulated through:

$$mult. \quad = \quad \frac{1}{N_{\rm tot}} \cdot \sum_{i=1}^{N_{\rm max}} i \times N_i\,, \tag{5}$$

where N_{tot} is the number of processed events, $N_{max} = 9$ is the maximum multiplicity in a 3×3 pad area, N_i is the number of events which showed a multiplicity of i. The error is given by:

$$\frac{\Delta mult.}{mult.} = \frac{\sum_i N_i}{\sum_i i \cdot N_i} + \frac{\Delta N_{\rm tot}}{N_{\rm tot}}\,. \tag{6}$$

Table 4 summarize the results for each chamber at a threshold of 1.5 fC.

Chamber	Raw mult.	Noise Corr. mult.
CH0	1.070±0.008	1.057±0.008
CH1	1.080±0.008	1.065±0.008
CH2	1.090±0.008	1.070±0.008
CH3	1.114±0.008	1.096±0.008

Table 4: Multiplicity measurements for a 1.5 fC threshold.

9 Threshold Dependencies

The chambers efficiency and the multiplicity at various thresholds have been measured and plotted in figure 14 and 16 respectively. The efficiency is falling down very quickly as the threshold increases. For a 20 fC threshold, the efficiency has already dropped to 70%. This shows the need for very low noise readout electronics if efficiencies abve 95% are needed for the DHCAL. This curve is no more than the integreal of the landau distribution substracted from 1. Using a higher gain shall then increase efficiency at high threshold.

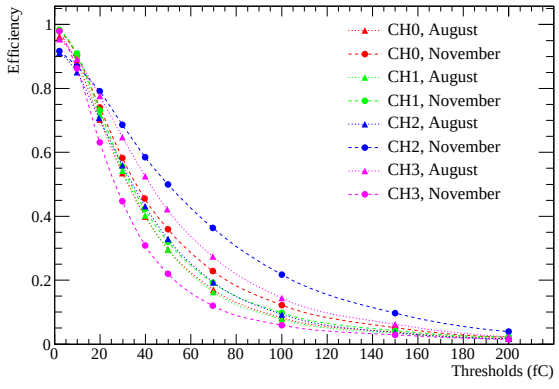

Figure 14: Efficiency versus threshold for every chamber and for both sessions.

Figure 15 shows the efficiency disparity versus the threshold. This parameter is of interest for

[5] For those hits the threshold has been be tuned from 1.5 to 200 fC.

[6] To minimize misalignment biases, a 3×3 pad area was preferred to a 1 pad one and the efficiency was only computed in a fiducial area omitting the border pads of the small detectors.

digital readout and for the PFA since it leads to some systematic uncertainties about the number of hits measured in the MICROMEGAS DHCAL. The trend is completely linear for threshold below 90 fC (0.15%/ fC). The lower plot of figure 15 confirms this trend for higher threshold but suffers from the low statistics at very low efficiency.

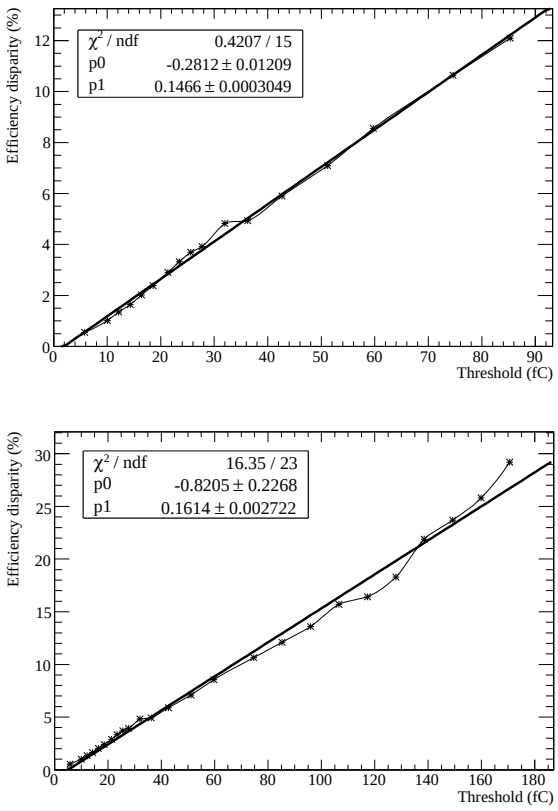

Figure 15: Efficiency disparity over 56 pads versus threshold for CH0. The upper plot for low threshold gives a precise value of this dependency (0.15%/ fC).

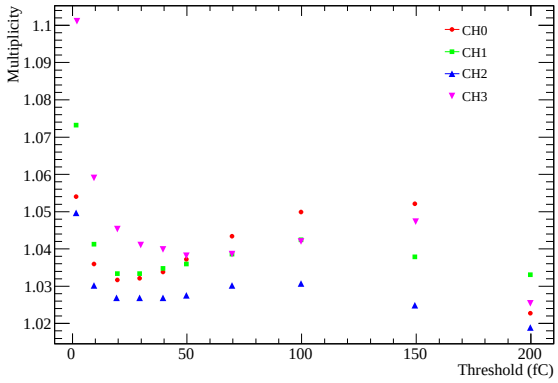

Figure 16: Multiplicity versus threshold for the four chambers.

The multiplicity shows a singular behaviour at first glance (see fig 16). After a quick fall, it rises slowly and then decreases at high threshold. At very low threshold, almost all hits are seen and the maximum multiplicity is measured. As the threshold increases, secondary hits due to small charge overflows (cross talk, electron avalanche spread ...) are quickly vanishing, thus inducing a swift fall of the multiplicity. As threshold keeps increasing, many low energy single hits are vanishing. Therefore, events with high energy δ rays, showing high energy deposition and high multiplicity, are taking higher weight in the computation of multiplicity. This argument explains the rise occurring roughly between 20 and 80 fC. For very high thresholds (above 150 fC), the multiplicity is decreasing again as expected.

10 Remarks about showers from 200 GeV/c pions

A 200 GeV/c pion beam from CERN/SPS/H2 line has been used to test the chambers in high energy dense hadronic showers. Iron blocks have been available to set a 30 cm thick wall upstream of the chambers to start showers. Considering a single channel allows to get rid of every chamber or readout disparity. Channel 38 has been chosen because it was the one gathering the most statistics under 200 GeV/c pion beam without absorber block before the detectors. This way, this channel response could be compared with the case when the absorber blocks were in place.

While taking data without absorber, the pions had very little probability to interact in the thin steel top of the chambers and thus behaved mostly like the muons. A Platinum Event folder with pion data has been built and a landau function has been fitted on single pad responses. The fit results showed no difference between pions and muons until the iron absorber blocks have been placed before the detectors stack (see table 5).

In the latter, the 30 cm thick iron wall, representing about 2 interaction lengths, provoked a shower in roughly more than 80% of the events. The interaction probability p is given by:

$$\begin{aligned} p &= 1 - e^{-x/\lambda} \\ &= 1 - e^{-2} \\ &= 0.86\,, \end{aligned}$$

where x is the absorber thickness and λ the interaction length.

200 GeV/c pion showers produce a high number of secondary particles in very dense jets. It is obvious that more than one particle crossed the same pad at once thus modifying the measured signal. On the one hand the combination of the deposited energy from several particles at the same time must enlarge the distribution. On the other hand, the showers have been produced with 200 GeV GeV/c, thus not at minimum ionization but on the relativistic rise with an average energy loss 50% higher than the minimum. Then, as the secondaries have to share the primary energy they have much lower energy and thus are much closer to minimum ionization (as illustrated on figure 17), that's why the distribution's MPV is lower in the case of showers.

The two first lines of table 5 show that the signal from pions is similar to the one from the muons. The last one gives the corresponding result in the case

Muons	MPV (ADU)	σ (ADU)
CH0	132.7±3.2	42.3±2.1
CH1	124.4±3.2	42.0±2.0
CH2	137.3±4.4	54.4±3.0
Pions	MPV(ADU)	σ(ADU)
CH0	130.0±2.7	40.8±1.7
CH1	122.4±2.6	42.5±1.7
CH2	137.7±3.4	51.1±2.2
Showers	MPV(ADU)	σ(ADU)
CH0	126.8±3.2	78.6±1.4
CH1	108.2±3.4	70.2±1.4
CH2	124.3±3.0	68.9±1.4

Table 5: Summary of the results given by the fit of a landau function on single pad signal for the three small chambers for three different situations.

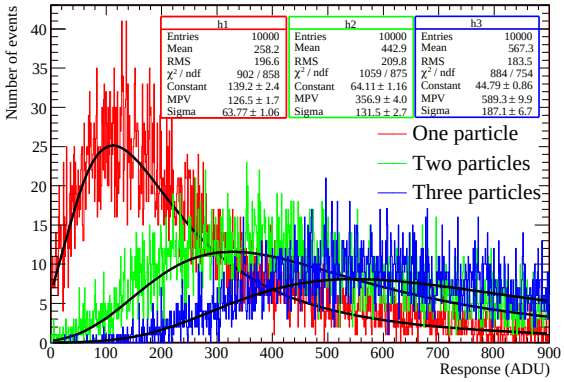

Figure 18: Distribution of energy loss for one, two and three particles at once in the same readout pad.

when pions interacted with the iron blocks placed in front of the chambers. In the two first cases, the σ of the distributions are identical for CH0 and CH1 and a little higher for CH3. In the shower case the σ are decreasing from CH0 to CH2, accordingly to their distance from the interaction point.

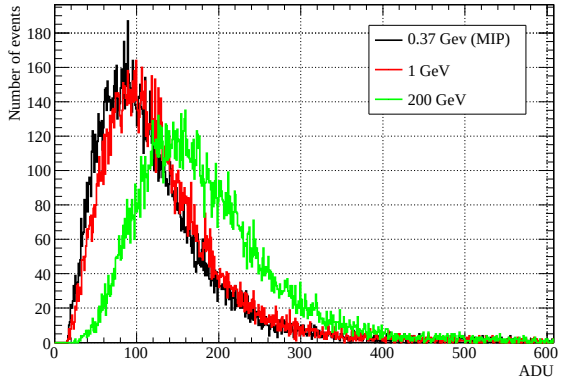

Figure 17: GEANT4 simulation of distribution of energy loss for muons crossing 3 mm of Ar/iC$_4$H$_{10}$ (95/5)

Figure 18 has been made using some toy Monte Carlo and shows the energy loss distribution of a single MIP crossing the detector (red curve). The one in green shows the energy loss distribution of two MIPs crossing the detector simultaneously and the black one is the same for three MIPs at once.

11 Conclusion

Four prototypes of MICROMEGAS chambers using bulk technology have been built and then tested in particle beams at CERN. Their gain disparity has been measured with an r.m.s. of 11%. Their efficiency has been measured near 97% with a disparity below 1% for a 1.5 fC threshold and showed a steep decline versus threshold whereas its disparity climbs slowly at 0.15% per fC threshold. The maximum multiplicity has been measured below 1.1 for all chambers at 1.5 fC threshold and showed a minimum of 1.03–1.04 around a threshold of 30–40 fC. An optimum may have to be found between efficiency and multiplicity. The global performances of those detectors are excellent. They're simple and robust. An operational ILC-designed MICROMEGAS-optimized digital embedded readout chip is needed to realize a functional ILC DHCAL active layer.

Contents

References

[1] Stephen R Magill, *Innovations in ILC detector design using a particle flow algorithm approach*, New Journal of Physics 9 (2007) 409, doi:10.1088/1367-2630/9/11/409.

[2] SiD, *Letter of Intent*, March 2009.

[3] I. Giomataris, Ph. Rebourgeard, J.P. Robert, G. Charpak, *MICROMEGAS: a high-granularity position-sensitive gaseous detector for high particle-flux environments*, Nuclear Instruments and Methods in Physics Research A 376 (1996) 29-35.

[4] I. Giomataris, R. De Oliveira, S. Andriamonje, S. Aune, G. Charpak, P. Colas, G. Fanourakis, E. Ferrer, A. Giganon, Ph. Rebourgeard, P. Salin, *MICROMEGAS in a bulk*, Nuclear Instruments and Methods in Physics Research A 560 (2006) 405-408.

[5] J.C. Santiard, K. Marent, *The Gassiplex0.7-2 Integrated Front-End Analog Processor for the HMPID and the Dimuon Spectrometer of ALICE*, 5th Conference on Electronics for LHC Experiments, Snowmass, CO, USA, 20 - 24 Sep 1999, pp.431-5.

[6] C. Adloff, M. Chefdeville, A. Espargilière, R. Gaglione, *Calibration of electronic readout chains for MICROMEGAS chambers*, LAPP Technical note, HAL : in2p3-00400295, 2009.

A Annex

A.1 Pedestal

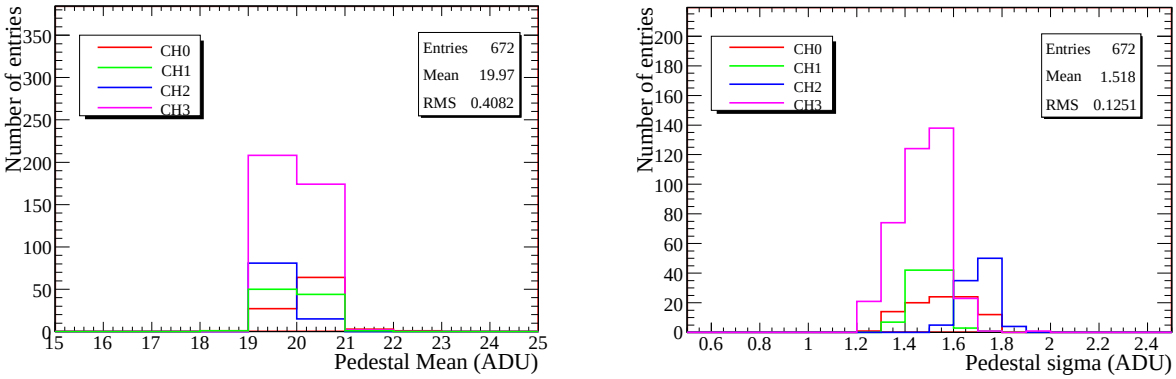

Figure 19: Pedestal Means (above) and sigmas (below).

A.2 Alignment

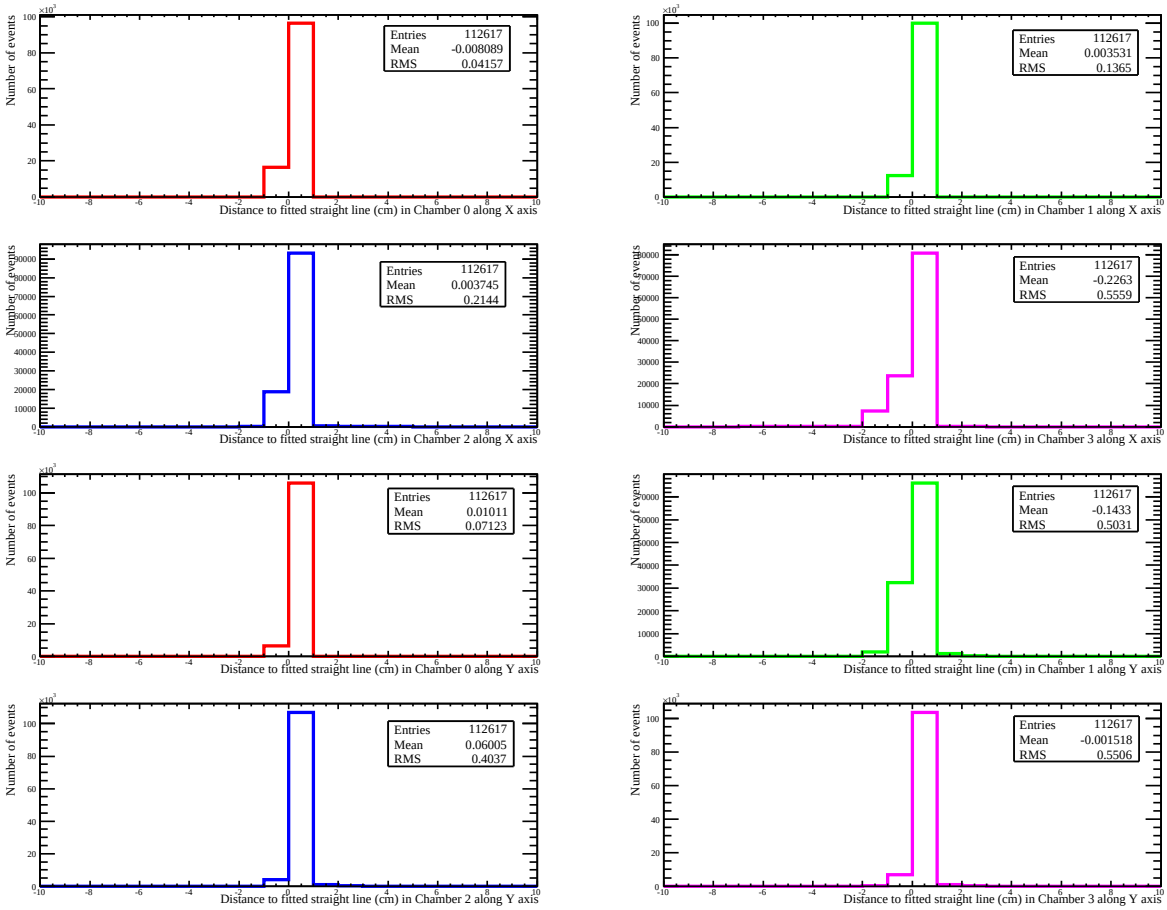

Figure 20: Measurement of all chambers relative misalignment.

A.3 Gain Plots

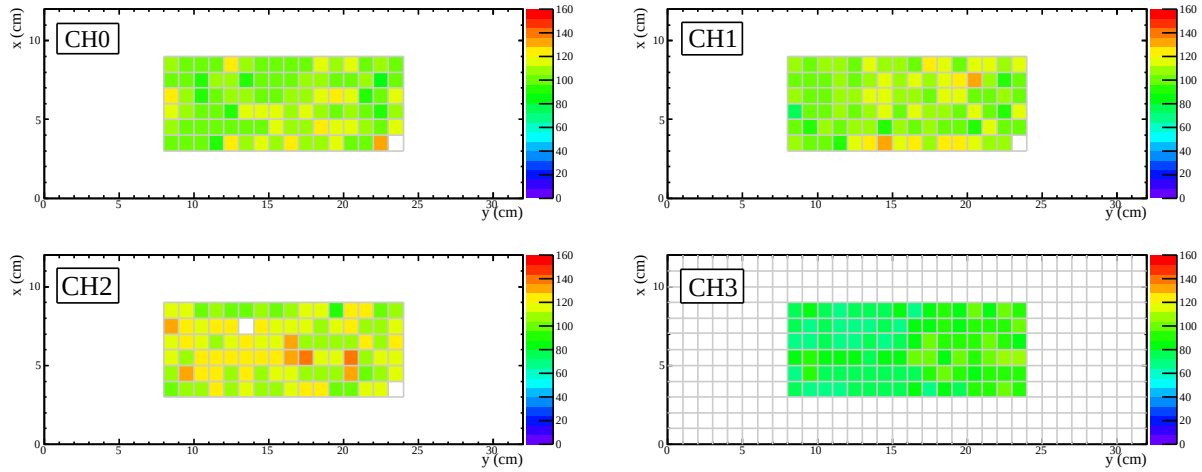

Figure 21: Maps of the four chambers' gains.

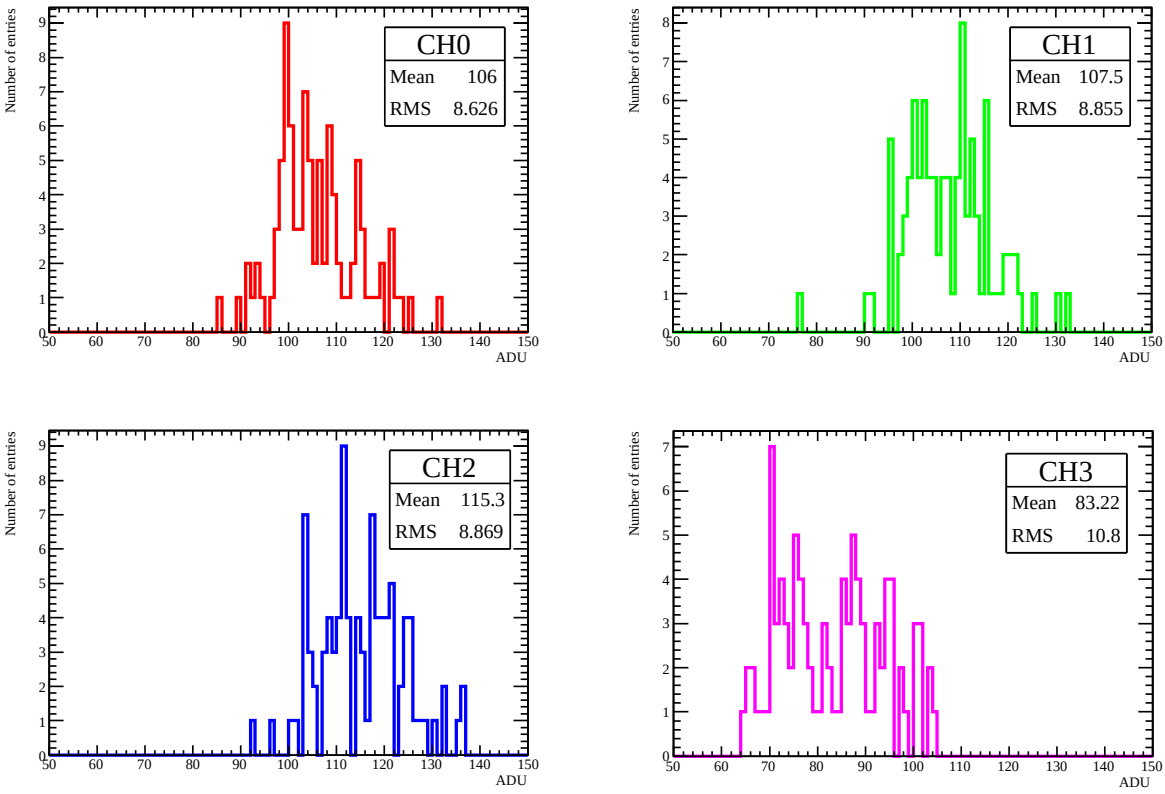

Figure 22: Histogram of each chamber's gain disparity

A.4 Efficiency Maps

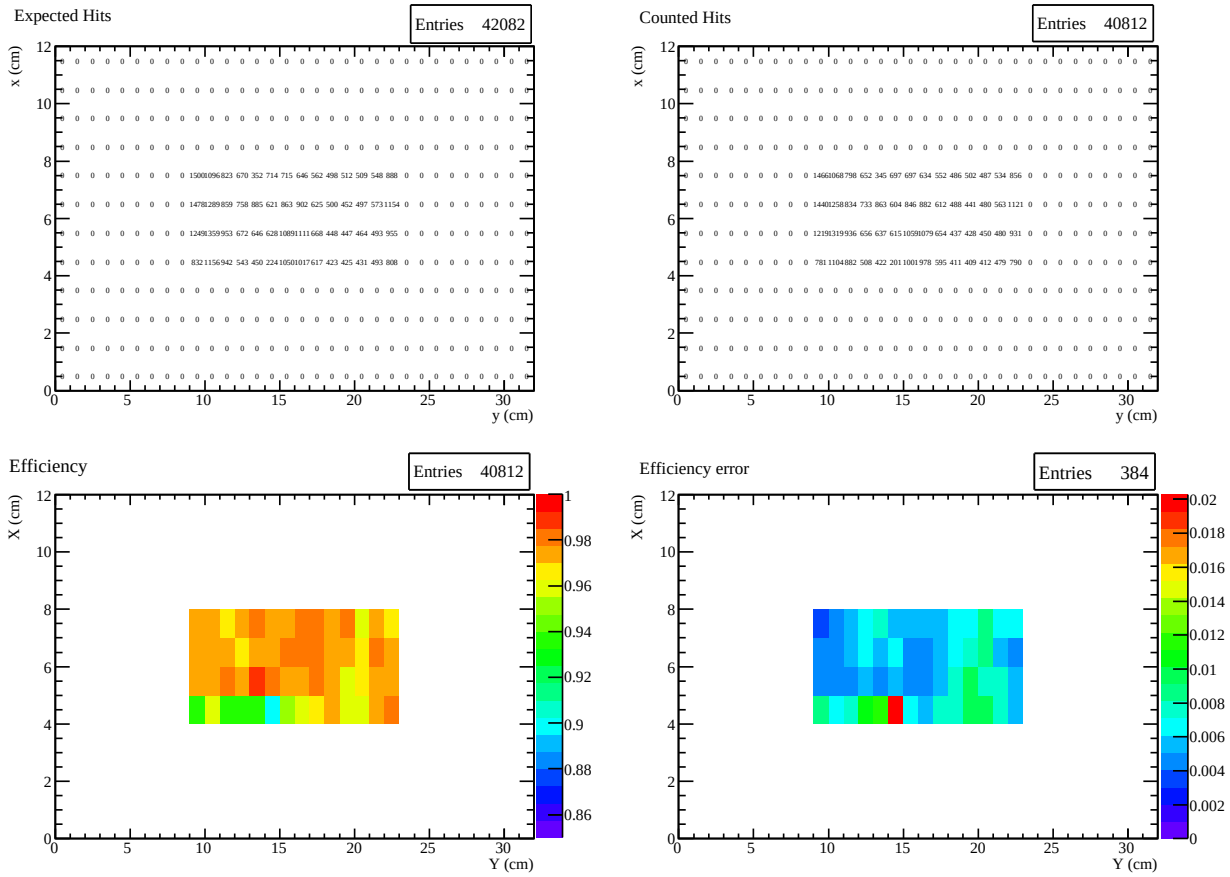

Figure 23: Efficiency map, principle of calculation.

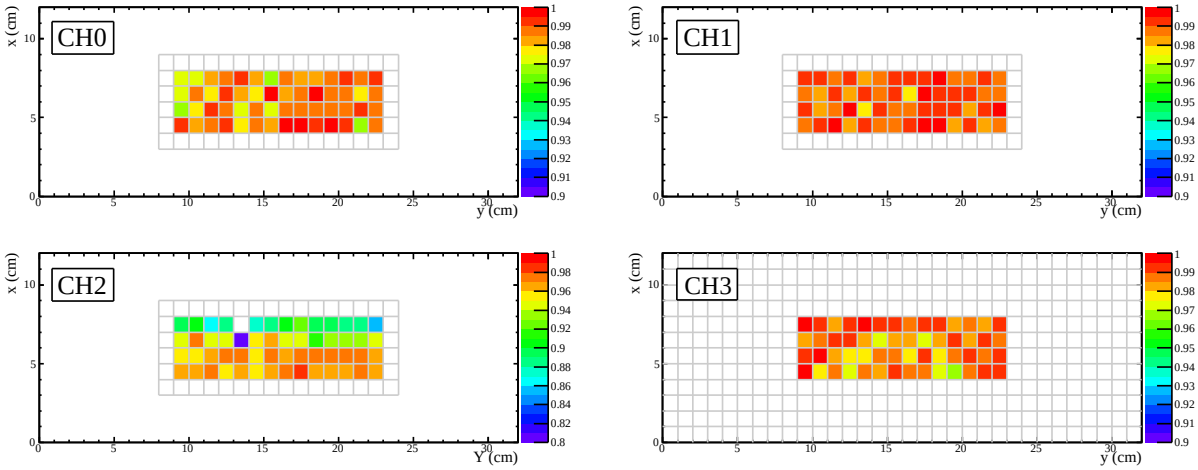

Figure 24: Efficiency maps of the four chambers.